HHS Public Access

Author manuscript

Nat Biomed Eng. Author manuscript; available in PMC 2017 December 08.

Published in final edited form as:

Nat Biomed Eng. 2017 ; 1: . doi:10.1038/s41551-017-0043.

Conformal phased surfaces for wireless powering of bioelectronic microdevices

Devansh R. Agrawal[1], **Yuji Tanabe**[2], **Desen Weng**[1], **Andrew Ma**[2], **Stephanie Hsu**[2], **Song-Yan Liao**[3], **Zhe Zhen**[3], **Zi-Yi Zhu**[3], **Chuanbowen Sun**[5], **Zhenya Dong**[5], **Fengyuan Yang**[5], **Hung Fat Tse**[3,4], **Ada S. Y. Poon**[2], and **John S. Ho**[1,5,*]

[1]Singapore Institute for Neurotechnology, National University of Singapore, Singapore

[2]Department of Electrical Engineering, Stanford University, CA 94305, USA

[3]Cardiology Division, Department of Medicine, University of Hong Kong, Hong Kong, China

[4]Hong Kong-Guangdong Joint Laboratory on Stem Cell and Regenerative Medicine, University of Hong Kong, Hong Kong, China

[5]Department of Electrical and Computer Engineering, National University of Singapore, Singapore

Abstract

Wireless powering could enable the long-term operation of advanced bioelectronic devices within the human body. Although both enhanced powering depth and device miniaturization can be achieved by shaping the field pattern within the body, existing electromagnetic structures do not provide the spatial phase control required to synthesize such patterns. Here, we describe the design and operation of conformal electromagnetic structures, termed phased surfaces, that interface with non-planar body surfaces and optimally modulate the phase response to enhance the performance of wireless powering. We demonstrate that the phased surfaces can wirelessly transfer energy across anatomically heterogeneous tissues in large animal models, powering miniaturized semiconductor devices (<12 mm^3) deep within the body (>4 cm). As an illustration of *in vivo* operation, we wirelessly regulated cardiac rhythm by powering miniaturized stimulators at multiple endocardial sites in a porcine animal model.

Bioelectronics offer sophisticated capabilities for physiological monitoring and modulation, but long-term powering of devices within the body remains a major technological challenge

*Correspondence and requests for materials should be addressed to J.S.H. (johnho@nus.edu.sg).
H.F.T., A.S.Y.P., and J.S.H. contributed equally as senior authors to the supervision of this work.

Code Availability: Custom scripts in MATLAB are available in the Supplementary Information.

Data Availability: The authors declare that all other data supporting the findings of this study are available within the paper and its supplementary information.

Author Contributions: D.R.A., Y.T., D.W., A.M., S.H., C.S., Z.D., F.Y., A.S.Y.P., and J.S.H. built and characterized the wireless powering system. Y.T., A.M., S.H., S.Y.L., Z.Z., Z.Y.Z., H.F.T., A.S.Y.P., and J.S.H. performed the *in vivo* experiments. D.R.A., H.F.T., A.S.Y.P., and J.S.H. wrote the manuscript.

Competing Financial Interests: This work relates to patent PCT/US2015/052642.

[1]. Batteries, for example, are bulky or have short lifetimes, while methods for harvesting physiological energy sources, such as vibrations [2] or thermal gradients [3], yield low power densities. Wireless powering has been extensively studied as a means to circumvent these limitations [4]. Most wirelessly powered bioelectronic systems, including commercial cochlear and retinal implants, are based on near-field coil pairs [5–9]. While well-suited for relatively large devices where dimensions are comparable to the transfer distance, miniaturization of the device is constrained because of weak coupling to the source, a consequence of the evanescent nature of the near-field.

An alternative approach is to exploit propagating fields in the electromagnetic midfield regime, where the wavelength λ is comparable to the transfer depth. In contrast to the near-field, the three-dimensional field pattern in this regime can be shaped by interference, allowing energy transfer to be enhanced by manipulation of the power flow lines [10, 11]. However, conventional field sources, such as antennas [12], cannot generate field patterns optimized for wireless powering because they lack control over the phase of the field. Phase modulation on body surfaces has so far relied on phased arrays in applications such as hyperthermia therapy [13] and microwave imaging [14]. Practical use of phased arrays in clinical settings, however, has been limited by their complexity and poor scalability. Systems demonstrated to date are bulky, requiring the patient to be completely immobilized, and achieve spatial resolutions too low ($\gg \lambda/10$) to optimally shape the field within the body [15–17]. In addition, existing systems rely on rigid interfaces with the body, preventing high-resolution control of phases on arbitrary body surfaces. We have previously used a four-element array to drive a patterned plate for wireless powering, but the implementation was rigid, required bulky control circuitry, and achieved limited resolution [11]. Although electromagnetic devices fabricated on flexible and stretchable substrates have recently been reported, the structures were designed for free-space radiation and do not control phase [18, 19].

Here, we demonstrate conformal electromagnetic structures, termed phased surfaces, that modulate phase with high resolution over non-planar body surfaces, and illustrate their capabilities in wirelessly powering microdevices. The structure is a metasurface [20, 21] comprising of reactively loaded rings that generate an engineered phase response optimized for energy transfer into the body. The phased surface does not require phase delay or control circuits, enabling its integration into a conformal device suitable for use on non-planar body surfaces. We use the phased surface to transfer energy across anatomically heterogeneous tissues, powering semiconductor microdevices (<12 mm^3) at depths inaccessible with conventional wireless powering systems.

System Overview

To optimally transfer energy in the midfield regime, theory has indicated that the source should induce convergence of power flow lines on a region deep in the body [10]. The region forms a diffraction-limited spot with width $\sim \lambda/n$, n the refractive index of tissue, where a microdevice can be efficiently powered. To create such a spot, the source must satisfy two criteria set by propagation constraints [21]. First, the source must generate a field with phase gradients larger than $2\pi/\lambda$ in order to access high wavevector ($k > 2\pi/\lambda$) components

required for subwavelength focusing. Exposed to air, the source thus emits an evanescent field with phase varying rapidly on a subwavelength scale. Second, the gap between the source and the body must be small over the active surface in order to allow efficient coupling through the evanescent field. Conventional phased arrays do not meet these criteria, being rigid and unable to accommodate subwavelength spacing. A previous study used a patterned metal plate for field shaping, but the structure was low-resolution, applicable only on flat surfaces, and required bulky phase delay circuitry [11].

We use the phased surface in Fig. 1a to meet these stringent electromagnetic requirements. Characteristic of a metasurface, the phases are engineered onto a surface using subwavelength resonant elements instead of propagation delays through materials or transmission lines. The phased surface (dimensions, 6 cm by 6 cm; weight, 11.2 g) was fabricated on a polyethylene terephthalate (PET) substrate (150 μm thickness) using a printed electronics process (Ag ink) and placed on soft polydimethylsiloxane (PDMS) spacer (3 mm thickness) capable of accommodating anatomical shapes and natural motion. Excitation of the center port by a continuous-wave signal induces oscillating currents in the rings, whose radiation and interference produce the field pattern (Fig. 2a). To tailor the phase of the currents, each ring is loaded with a reactive element (0.2 to 1 pF capacitor, Supplementary Fig. S1) that creates a resonance near the driving frequency [22, 23]. Across each resonance, the current phase transitions between leading and lagging the driving signal by $\pi/2$. By coupling multiple resonances through the mutual impedances between the rings, the phase difference can cover the entire 2π range (Fig. 2b). An extensive numerical scheme is used to solve for the optimal set of currents shown in Fig. 2a (see Methods, Supplementary Fig. S2) and the corresponding reactive elements. The resulting structure focuses energy to a target region 4.5 cm deep in body when conformally placed on the body surface (Fig. 1b).

As a demonstrative device, we designed a light-emitting microdevice using commercial semiconductor components. The microdevice consists of a helical coil (1.5 mm diameter, 3 mm length) mounted on a circuit board (FR4, 270 μm thickness) containing a rectifying circuit and a light-emitting diode (LED, blue 475 nm) (Fig. 1c,d and Supplementary Fig. S3). The coil is tuned to resonance by the input capacitance of the rectifying circuit. After encapsulation in transparent silicone, the microdevice is 12 mm^3 and weighs 20 mg. During power measurements, the microdevice is mounted on the tip of an optical fiber to monitor the emitted light and facilitate placement within the body (Supplementary Fig. S4). The optical signaling modality eliminates measurement error due to metallic scattering if wire probes or test connectors are used. Larger versions of the device could increase energy extraction from the incident field, although we show that clinically relevant operation of these miniaturized devices deep in the body is possible within an optimally shaped field.

Because the phases are fixed, enhanced performance relies on conservation of the field shape across a range of anatomically heterogenous tissues. The field shape can be robust to the composition of the intervening tissue because of the relative homogeneity of the tissue permittivities at the operating frequency (Supplementary Table 1) and diffraction originating from the long wavelength (λ_{muscle} = 2.5 cm). Characteristic of wireless systems, the relative position of the source and the receiver is an important factor in performance, and spatial

focusing of the field increases sensitivity to an extent. We demonstrate wireless powering over a clinically relevant range of tissue structures, source-receiver geometries, and physiological motions.

Results

System characterization

We characterized the wireless powering system in both tissue-mimicking liquid and in multilayered animal tissue. Simulations, field mapping, and wireless powering experiments (Fig. 2c,d,e) demonstrate that the phased surface produces a strongly focused field in homogenous media (saline in experiments, homogeneous muscle tissue in simulations), transferring 0.83 mW to the microdevice over 4 cm of saline at 800 mW output (Fig. 2f and Supplementary Fig. S5). In multilayered porcine tissue, both simulation and experiment show that 0.45 mW was transferred over 4.2 cm (Fig. 2e,f). For a microdevice in this source-receiver configuration, these transfer efficiencies are about two orders of magnitude greater than those achieved in the near-field by the theoretical optimal source [10], and meets requirements for many bioelectronic sensing and modulation systems. For comparison, analog cochlear processors consume 0.2 mW and pacemakers less than 0.01 mW on average [1]. Phase control is key to performance, as removal of the reactive loading elements on the phased surface destroys the focal spot, reducing the transferred power fivefold at the 4 cm depth (Fig. 2c,f). In contrast, replacing homogenous media with multilayered tissue reduced the transferred power by less than twofold.

A distinctive feature of the phased surface is that it couples energy into the body with high efficiency and selectivity ($>$96% of outgoing power), strongly suppressing radiation into free-space. Fig. 2f shows that over a 4 cm range from the phased surface, the received power is nearly an order of magnitude less in air than in tissue, even though dissipative losses occur only in tissue. For a microdevice requiring 0.5 mW for function, the device can be powered at a depth of 4.6 cm in a field optimized in muscle tissue, compared to 1.2 cm in air. This counterintuitive result highlights the essential role of propagating fields in transporting energy: the enhanced range is a consequence of evanescent-to-propagating field conversion at the air-tissue interface and subsequent interference with the prescribed phases. The conformal design of the phased surface is essential because a rigid device does not provide effective coupling to the body on curved body interfaces (Supplementary Fig. S6).

Stability of the coupling between the phased surface and the body was tested under deformation and physiological movement. Field mapping measurements show that the field shape is maintained for interfaces with radii-of-curvature greater than 8 cm, which should accommodate most non-peripheral body surfaces (Supplementary Fig. S6). Measurements of the scattering parameters on three human subjects with the phased surface attached by Tegaderm film on the chest and leg show that the coupled power varies by less than 0.02% during the physiological motions of sitting, standing, and walking (Supplementary Fig. S7). In contrast, removal of the phased surface beyond 4 cm distance results in a 7% change in power. No significant changes in the conductivity of the Ag traces were observed across the range of physiologically relevant curvatures (Supplementary Fig. S8). The coupling is also relatively stable across a wide range of PDMS substrate thicknesses greater than 2 mm

(Supplementary Fig. S9). These results show that the conformal design enables robust electromagnetic coupling with the body, although matching its mechanical properties to that of skin remains an important direction for future work.

We measured the dependence of performance on source-receiver geometry for the wireless powering configuration in Fig. 3a. Because energy transfer is mediated by propagating fields, the dependencies on linear displacement are determined solely by the spatial distribution of the field; the half-power displacements are 11.5 mm in the transverse plane and 6.7 mm in depth (Fig. 3b,c). The orthogonal electric and magnetic components of the generated field interact with both the electric and magnetic dipole moments of the helical receiver. Power can thus be extracted for all azimuthal orientations θ without nulls (Fig. 3d, Supplementary Fig. S10a), while the altitudinal angle ϕ follows a cosine dependence (Fig. 3e, Supplementary Fig. S10b) (half-power displacement: 59° azimuthal and 45° altitudinal). These displacements quantify the sensitivity of performance to changes in source-receiver alignment due to movement of the phased surface or the device, or both. In contrast to near-field systems, operation in the midfield is immune to frequency-splitting effects, and the overall dependencies are less than or similar to previously reported systems [24].

Safety characteristics were also studied computationally and experimentally. Simulations on a computational human torso show that at an output power of 800 mW, the dissipated power is localized to the area under the phased surface with peak specific absorption rate (SAR) of 8.9 W/kg, averaged over 10 g of tissue (Fig. 3f). This value is below the 10 W/kg threshold, under which no adverse effects have been established [25]. SAR levels observed for arm and neck configurations are also below this threshold (Supplementary Fig. S11). To assess direct thermal effects, operation of the phased surface on the human body was further studied. Thermal imaging on the human abdomen showed that the temperature increase attributable to the radio-frequency (RF) heating is about 1°C over 6 min of continuous exposure at 800 mW (Fig. 3g,h), and are comparable on the arm and neck (Supplementary Fig. S12). SAR profiles show that the dissipation is localized near the surface, reaching half the peak value approximately 2 cm from the surface. In applications where the microdevice is powered in a pulsatile rather than continuous manner, such as neural or muscular stimulation, the average exposure will be lowered by the duty cycle. These preliminary studies suggest that the system can safely power microdevices, although further studies will be needed in order to weigh risk of RF exposure against potential clinical benefits.

Wireless powering of implanted microdevices

We characterized the performance of the system by wirelessly powering microdevices implanted in adult pig (male, 70 kg) viscera and neck. The microdevice was inserted into the body by tunneling the optical fiber into the peritoneal cavity while the phased surface was placed over the device on the body surface. Initial placement of the phased surface relied on feedback from the microdevice; no imaging guidance was used. Once the surface placement was determined, wireless powering of the device was repeatable and tolerant to placement ($\pm$1 cm). Computed tomography (CT) shows relative positions of the phased surface and the implanted microdevice (Fig. 4a,b) in three configurations: (i) right upper quadrant and (ii) right lower quadrant of the abdomen, with microdevice implanted in the peritoneal cavity,

and (iii) right neck surface, with microdevice implanted in the carotid sheath. The depth of implantation ranges from 3.8 to 4.1 cm from the surface (Fig. 4c). The power received in each configuration is about 0.6 mW at 800 mW continuous power (Fig. 4d,e) with profile, traced along the trajectory of optical fiber, showing localization of energy to a spot with width varying from 1.8 cm (0.096λ) to 2.8 cm (0.149λ) (Fig. 4f). The width of the profile measured in the upper abdomen is slightly narrower than the width predicted in homogenous tissue, likely due to small distortion of the field shape across the rib cage. Note that the thicknesses of the porcine tissues evaluated here are significantly greater that the corresponding human average. Optical power densities above 1 mW/mm^2 (Supplementary Fig. S4b) can be generated under safe average exposure levels if the duty cycle is below 50%, which meets requirements for use in applications such as optogenetics [26].

We also studied the effect of bone structures on energy transfer. Power was wirelessly transferred across the rib cage in the upper abdomen configuration (Fig. 4a). The received power profile (Fig. 4d) has performance and symmetry comparable to that of the lower abdomen and neck configurations, which do not contain bone. Computational studies show that the received power decreases by a maximum of 13% when the microdevice behind a rib-like (1 cm width) structure in otherwise homogenous tissue (Supplementary Fig. S13a,b,d,e). Reflection increases the received power slightly when bone is present behind the microdevice. The robustness of wireless powering to bone is a result of the relatively low impedance mismatch between bone and soft tissue ($\lambda_{bone}/\lambda_{muscle} \approx 1.6$) and diffraction due to the long wavelength ($\lambda_{muscle} = 2.5$ cm) relative to the dimensions of the bone. Layered bone structures at thicknesses comparable to the human skull (less than 1 cm) cause slight broadening of the field shape, although reduced absorption results in overall increase in received power (Supplementary Fig. S13c,f). These results demonstrate the potential of the phased surfaces to power devices in regions difficult to access through modalities with high bone contrast, such as ultrasound.

We next illustrate operation of the phased surface *in-vivo* by wirelessly powering a miniaturized stimulator for cardiac pacing. The stimulator, shown in Fig. 5a, consists of the microdevice attached to pacing electrodes, yielding a cylindrical device 1.5 mm in diameter and 5 mm in length. The dimensions of the helical coil are consistent with prior experiments. The stimulator was mounted on the tip of a deflectable transvenous catheter and inserted at endocardial stimulation sites in the left ventricle (LV), right atrium (RA), and the right ventricle (RV) (Fig. 5b–d). The stimulation voltage waveform (10 ms width, 600 ms period) was generated by pulsed radio-frequency excitation of the phased surface, which produces minimal distortion because of its relatively large bandwidth (60 MHz, Supplemental Fig. S14). Fig. 5e shows representative electrocardiogram (ECG) recordings during 10-s stimulation/rest intervals for each stimulation site. The heart rate is elevated to the target rate following 2 to 4 seconds of stimulation, immediately returning to baseline once the stimulation pulses cease (Fig. 5f). Different target rates were also achieved at the same site (Supplementary Fig. S15). The minimum average power levels required to successfully pace the heart were 216 mW (LV), 34 mW (RA), and 108 mW (RV), which are well below the previously established safety thresholds. The variability in required power is likely due to the different depths of the stimulation sites as well as the excitability of the target tissue. Continuous operation of the device will require methods to achieve long-term reliability,

such as through integration of rechargeable energy storage components [27]. These results, however, indicate that the performance levels are sufficient for microdevices to wirelessly elicit temporary physiological effects from deep organs on demand. Bioelectronic modulation of physiological function through neural stimulation or drug release could provide therapeutic effect in this mode.

Clinical applications of the system may benefit from a portable or wearable wireless powering source. In contrast to phased arrays, the RF components required to drive the phased surface are minimal and can readily be integrated. Supplementary Fig. S16 shows an example in which commercial RF integrated circuits (oscillator and power amplifier) and a battery are mounted behind a rigid phased surface. The components do not significantly affect the field shape and the focal spot generated from a flat surface is nearly identical to the tethered source. The integrated device can achieve a maximum output power is 1 W, which is sufficient to reach the continuous SAR-limited output. The substrate choice is currently limited by the rigid components; integration of commercial components with overall flexible mechanics represents an important direction for future work.

Discussion

We have demonstrated conformal electromagnetic structures capable of wirelessly powering microdevices implanted deep in the body. In contrast to prior approaches based on phased arrays, the phases are engineered into these surfaces using subwavelength resonant elements, enabling higher resolution and integration into a conformal device. These capabilities enhance wireless powering performance by enabling the field in the body to be optimally shaped from non-planar body surfaces. Experiments in large animal models show enhanced performance across a physiologically relevant range of heterogenous tissues, geometrical displacements, and motions. The variation in performance with these parameters, however, is significant (at least comparable to existing wireless powering systems) and mitigating these sensitivities is an important research direction. Reconfigurable structures that exploit wireless feedback from the microdevice, for example, could adaptively shape the field to reduce sensitivity to displacements, using similar methods to achieve high phase resolution.

Beyond the illustrative example of cardiac pacing, clinical applications of wireless powering may be most immediately promising for emerging applications that operate on-demand rather than continuously. In particular, the ability of the phased surfaces to wirelessly power microdevices at deep organ or tissue sites could provide important capabiltiies for neuromodulation [28], drug delivery, and other therapies based on wireless delivery of light, heat, or electrical pulses.

The phased surfaces should also, by reciprocity, provide high performance in the receiving mode, and could be used to enhance signal reception from deep sensors and monitoring devices. By engineering the combined amplitude, phase, and polarization response [29, 30], we also anticipate that similar structures could further enhance wireless powering performance and robustness.

Methods

Phased surface design

Optimal current amplitudes and phases were determined by solving a matched filter problem for a prescribed powering depth in homogenous tissue, taken to have the permittivity of muscle [31]. Following the procedure described in Ref. [21], the input port, the elements on the metasurface, and the receive structure are regarded as a multiport system. The scattering matrix for the system is computationally obtained using a model of the flat phased surface over muscle tissue with a receiver (2 mm diameter wire loop) placed at a 4.5 cm depth (CST Microwave Suite). The matrix is partitioned as

$$\begin{pmatrix} \vec{b}_S \\ b_R \end{pmatrix} = \begin{pmatrix} \sum_S & \vec{\kappa} \\ \vec{\kappa}^T & \sigma_L \end{pmatrix} \begin{pmatrix} \vec{a}_S \\ a_R \end{pmatrix} \quad (1)$$

where $\vec{b}_S$ ($\vec{a}_S$) are the backward (forward) wave amplitudes at the source and b_R, a_R the respective amplitudes at the receiver. The forward amplitudes maximizing power transferred to the load are given by the matched filter

$$\vec{a}_{S,\mathrm{opt}} = \left[I - \sum\nolimits_S^H \sum\nolimits_S - \vec{\kappa}\vec{\kappa}^H \right]^{-1} \vec{\kappa}^*. \quad (2)$$

The inverse exists since the bracketed matrix is required by energy conservation to be positive definite. The reactive loading elements that generate these amplitudes and phases were selected by an optimization algorithm (see Supplementary Information: Additional Methods).

Wireless powering system

An RF signal generator (Berkeley Nucleonics, Model 835) with a power amplifier (Mini Circuits, ZHL-10W-2G+) provides energy to the phased surface. The signal generator is connected to the power amplifier by a RF coaxial cable (SMA-SMA, 50 Ω, Amphenol). The amplifier (pre-mounted on a heatsink and fan) is powered by a separate power supply unit (Tektronix, PWS2326). The power amplifier is connected to the transmitter using a coaxial and an adaptor cable (SMA-MMCX, 50 Ω, Amphenol). The end-to-end gain between the signal generator and the transmitter is measured to be 42 dB at 1.6 GHz.

Large animal experiment

Experiments used an adult male pig (70 kg) model in the National Large Animals Research Facility. Measurements were performed with 2 hours of euthanasia. Laparotomy was performed to insert the microdevice mounted on an optical fiber into the abdominal cavity. In the neck configuration, a vertical incision was made in the lower neck to gain access to the carotid sheath. These experiments were approved by National University of Singapore Comparative Medicine.

On-body evaluation

For mechanical evaluation during physiological motion, three healthy subjects were recruited. During each trial, the phased surface was first placed on the chest and then the leg of the volunteer. The device was secured on to the skin with Tegaderm film and connected to a vector network analyzer (VNA, Keysight Field-Fox) with a coaxial cable held slack. The VNA was set to monitor the reflected power in continuous acquisition mode. The volunteers performed physiological motion by transitioning between sitting to standing and standing to walking. For thermal evaluation, a single healthy subject was recruited. A volunteer reclined in a chair while the phased surface was fixed over test surface (abdomen, neck, and arm) by temporary adhesive to reduce movement. Infrared thermal images (E5, FLIR Systems) were acquired during brief intervals during which the phased surface is removed from the surface. The duration where the phased surface was not in contact with the skin was not counted towards the elapsed time. Calculation of the temperature increase followed method described in Supplementary Information: Additional Methods. The study was approved by the National University of Singapore Institutional Review Board (NUS-IRB). All subjects were volunteers for this study, were informed of risks and benefits, and provided informed consent.

Cardiac pacing experiment

Cardiac pacing experiments used an adult female pig (45 kg). The animal was anesthetized induced with tiletamine and zolezepam (Zoletil, 20 mg/kg) and maintained with isoflurane (1.5% to 2.0%). Endotracheal intubation was performed to provide mechanical ventilation. Surface electrocardiogram recordings were performed with electrodes placed on the limbs and a digital recording system (CardioLab, GE Healthcare). The stimulator was assembled by cutting a commercial deflectable quadripolar electrode catheter (A-Josephson type, Biosense Webster, Johnson and Johnson) and soldering the exposed wires across the LED pads of the microdevice. The stimulator was attached to the tip of a catheter and inserted into the heart through an introducer in the femoral vein or artery. Positioning at the selected endocardial sites was performed under fluoroscopic guidance. All animal experiments were conformed to the Guide for the Care and Use of Laboratory Animals published by the US National Institutes of Health and the study protocol was approved by the local institutional ethics committee for animal research.

Supplementary Material

Refer to Web version on PubMed Central for supplementary material.

Acknowledgments

We acknowledge support from grants from the Singapore Institute for Neurotechnology, US National Science Foundation (ECCS-1351687), the US National Institutes of Health (National Institute of Biomedical Imaging and Bioengineering grant R21EB020894), and the Hong Kong Innovation and Technology Fund (ITS/087/14).

References

1. Chandrakasan AP, Verma N, Daly DC. Ultralow-power electronics for biomedical applications. Annu Rev Biomed Eng. 2008; 10:247–274. [PubMed: 18647116]

2. Dagdeviren C, et al. Conformal piezoelectric energy harvesting and storage from motions of the heart, lung, and diaphragm. Proc Natl Acad Sci, USA. 2014; 111:1927–1932. [PubMed: 24449853]
3. Leonov V. Thermoelectric energy harvesting of human body heat for wearable sensors. IEEE Sensors J. 2013; 13:2284–2291.
4. Schuder J, Stephenson H Jr, Townsend J. High level electromagnetic energy transfer through a closed chest wall. Inst Radio Engrs Int Conv Record. 1961; 9:119–126.
5. Jow UM, Ghovanloo M. Design and optimization of printed spiral coils for efficient transcutaneous inductive power transmission. IEEE Trans Biomed Circuits Syst. 2008; 1:193–202.
6. Liu W, et al. A neuro-stimulus chip with telemetry unit for retinal prosthetic device. IEEE J Solid-State Circuits. 2000; 35:1487–1497.
7. RamRakhyani AK, Mirabbasi S, Chiao M. Design and optimization of resonance-based efficient wireless power delivery systems for biomedical implants. IEEE Trans Biomed Circuits Syst. 2011; 5:48–63. [PubMed: 23850978]
8. Waters BH, Sample AP, Bonde P, Smith JR. Powering a ventricular assist device (VAD) with the free-range resonant electrical energy delivery (FREED) system. Proc IEEE. 2012; 100:138–149.
9. Ahn D, Ghovanloo M. Optimal design of wireless power transmission links for millimeter-sized biomedical implants. IEEE Trans Biomed Circuits Syst. 2016; 10:125–137. [PubMed: 25616074]
10. Kim S, Ho JS, Poon ASY. Midfield wireless powering of subwavelength autonomous devices. Phys Rev Lett. 2013; 110:203905. [PubMed: 25167413]
11. Ho JS, et al. Wireless power transfer to deep-tissue microimplants. Proc Natl Acad Sci, USA. 2014; 111:7974–7979. [PubMed: 24843161]
12. Chow EY, et al. Wireless powering and the study of rf propagation through ocular tissue for development of implantable sensors. IEEE Trans Antennas Propag. 2011; 59:2379–2387.
13. Ling H, Lee SW. Focusing of electromagnetic waves through a dielectric interface. J Opt Soc Am A. 1984; 1:965–973.
14. Li X, Davis SK, Hagness SC, vanderWeide DW, VanVeen BD. Microwave imaging via space–time beamforming: Experimental investigation of tumor detection in multilayer breast phantoms. IEEE Trans Microwave Theory Techn. 2004; 52:1856–1865.
15. Ling H, Lee S, Gee W. Frequency optimization of focused microwave hyperthermia applicators. Proc IEEE. 1984; 72:224–225.
16. Meaney PM, Fanning MW, Li D. A clinical prototype for active microwave imaging of the breast. IEEE Trans Microwave Theory Tech. 2000; 48:1841–1853.
17. Wu L, McGough RJ, Arabe OA, Samulski TV. An RF phased array applicator designed for hyperthermia breast cancer treatments. Phys Med Biol. 2005; 51:1–20. [PubMed: 16357427]
18. Xu S, et al. Soft microfluidic assemblies of sensors, circuits, and radios for the skin. Science. 2014; 344:70–74. [PubMed: 24700852]
19. Hussain AM, et al. Metal/polymer based stretchable antenna for constant frequency far-field communication in wearable electronics. Adv Funct Mater. 2015; 25:6565–6575.
20. Yu N, Capasso F. Flat optics with designer metasurfaces. Nat Mater. 2014; 13:139–150. [PubMed: 24452357]
21. Ho JS, et al. Planar immersion lens with metasurfaces. Phys Rev B. 2015; 91:125145–8.
22. Harrington RF. Reactively controlled directive arrays. IEEE Trans Antennas Propag. 1978; 26:390–395.
23. Grbic A, Merlin R, Thomas EM, Imani MF. Near-field plates: Metamaterial surfaces/arrays for subwavelength focusing and probing. Proc IEEE. 2011; 99:1806–1815.
24. Ozeki T, et al. Functions for detecting malposition of transcutaneous energy transmission coils. ASAIO Journal. 2003; 49:469–474. [PubMed: 12918593]
25. IEEE Standard C95.1. IEEE Standard for Safety Levels with Respect to Human Exposure to Radio Frequency Electromagnetic Fields, 3 kHz to 300 GHz. 2005
26. Montgomery KL, et al. Wirelessly powered, fully internal optogenetics for brain, spinal and peripheral circuits in mice. Nat Methods. 2015; 12:969–974. [PubMed: 26280330]
27. Meng C, Maeng J, John SWM, Irazoqui PP. Ultrasmall integrated 3d micro-supercapacitors solve energy storage for miniature devices. Adv Energy Mater. 2013; 4:1301269.

28. Birmingham K, et al. Bioelectronic medicines: a research roadmap. Nat Rev Drug Discov. 2014; 13:399–400. [PubMed: 24875080]

29. Zhao Y, Alu A. Manipulating light polarization with ultrathin plasmonic metasurfaces. Phys Rev B. 2011; 84:205428–6.

30. Pfeiffer C, Grbic A. Metamaterial huygens' surfaces: Tailoring wave fronts with reflectionless sheets. Phys Rev Lett. 2013; 110:197401–5. [PubMed: 23705738]

31. Gabriel S, Lau RW, Gabriel C. The dielectric properties of biological tissues: III. Parametric models for the dielectric spectrum of tissues. Phys Med Biol. 1996:2271–2293. [PubMed: 8938026]

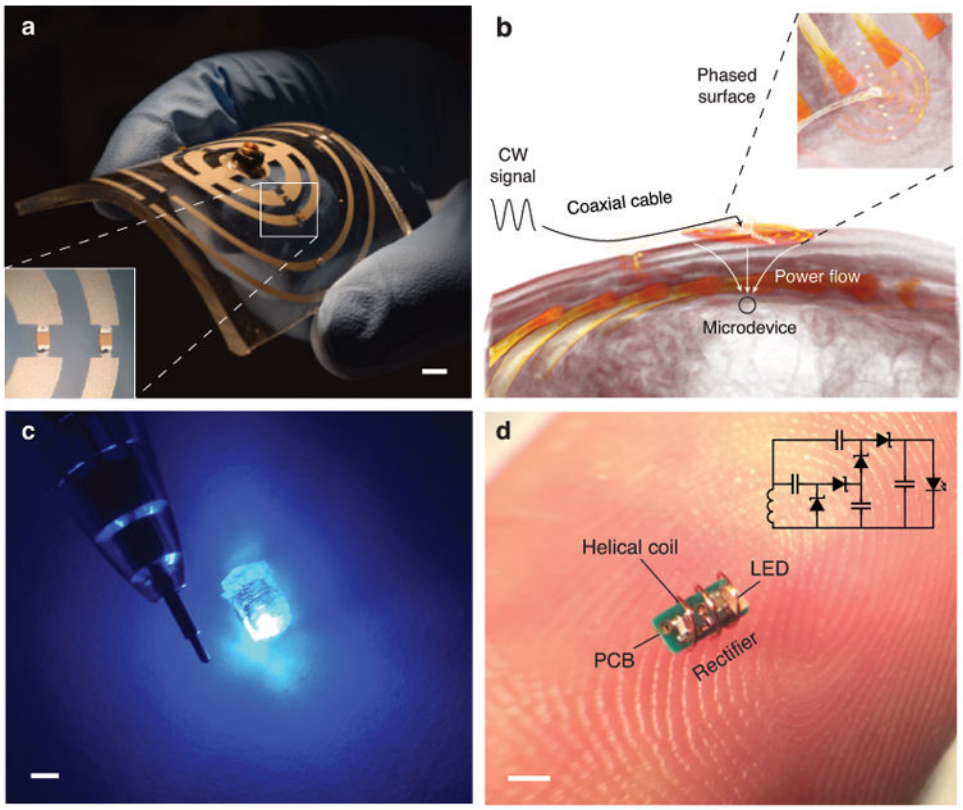

Fig. 1.

Phased surface wireless powering system. (a) Image of the phased surface in a curved state. Inset shows micrograph of the reactive elements loading each ring. Scale bar, 1 cm. (b) Schematic of the wireless powering system for powering an implanted microdevice. (c) Light-emitting microdevice shown next to pencil tip for size comparison. Scale bar, 1 mm. (d) Image of microdevice prior to encapsulation on human index finger. The inset shows the circuit diagram. Scale bar, 1 mm.

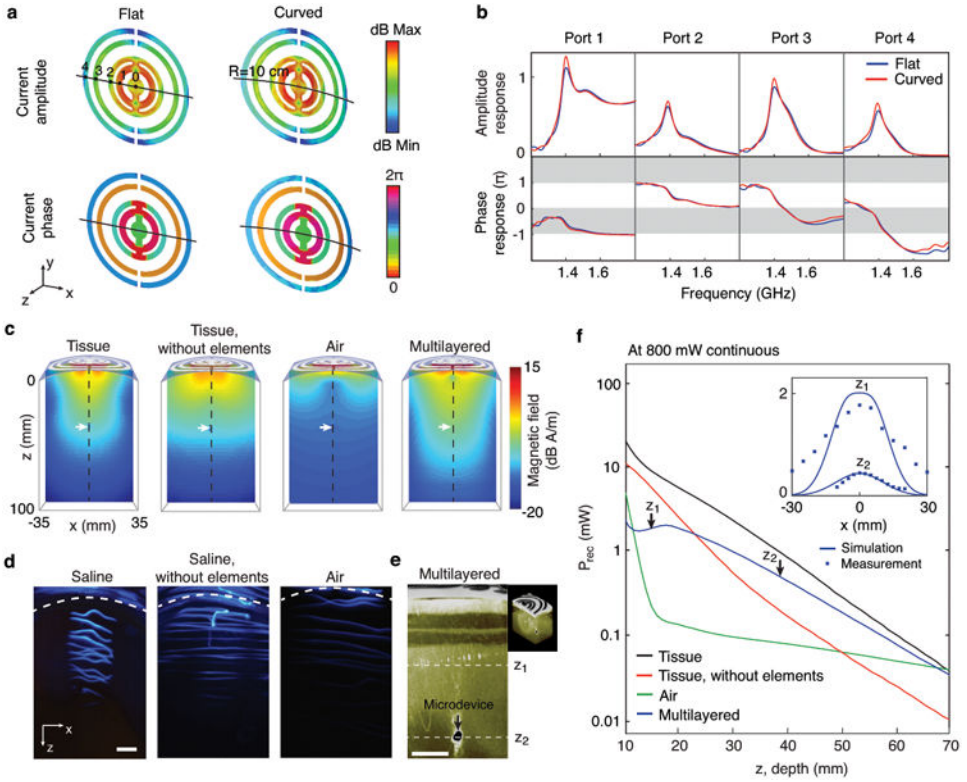

Fig. 2.

Wireless powering performance of the phased surface. (a) Amplitude and phase distribution of the surface current during continuous-wave excitation, in flat and curved (radius of curvature $R = 10$ cm) states. Ports 0, 1, 2, 3, and 4 are labeled. (b) Amplitude and phase response as a function of frequency. The response is defined as I_n/I_0, where I_n is the current flowing through port n. (c) Simulated magnetic field intensity generated by the phased surface above tissue, without reactive loading elements, in air, and above tissue multilayers. The microdevice is placed at a 4.5 cm depth (white arrow). Tissue consists of homogenous muscle while multilayers consist of skin (3.2 mm thick), fat (8 mm thick), and muscle (remaining space). (d) Time-lapse images as a microdevice is moved under the phased surface in the configurations in (c). Scale bar, 1 cm. (e) Computed tomography image of the multilayered explanted porcine tissue. Inset shows phased surface above the tissue. Scale bar, 1 cm. (f) Power received by the microdevice as a function of depth at an output power of 800 mW. Inset shows the measured received power in multilayer tissue at depths z_1 =15 mm and z_2 = 42 mm.

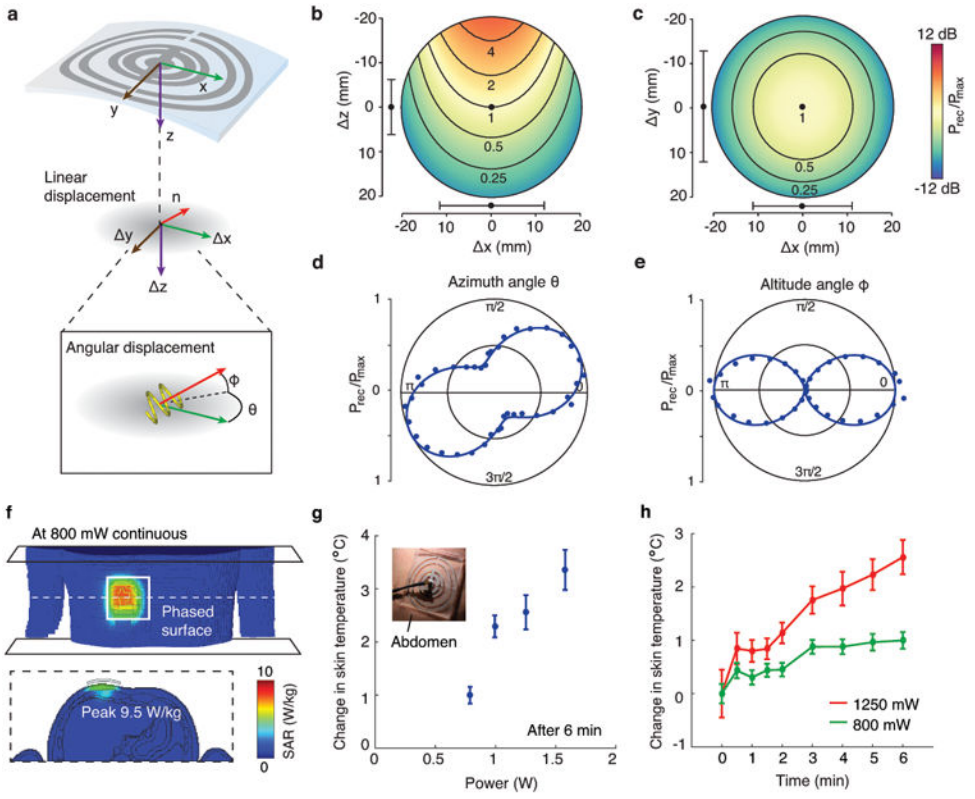

Fig. 3.

Performance variation with geometry and thermal characteristics. (a) Wireless powering configuration with linear and angular displacement. The space below the phased surface is assumed to be homogenous muscle tissue. (b,c) Simulated contour plot of normalized received power with linear displacements (b) Δx and Δz, and (c) Δx and Δy. The lines above the axes show the corresponding half-power displacements measured in saline. (d,e) Polar plot of the normalized received power with angular displacements (d) $\Delta\theta$ and (e) $\Delta\phi$ and theoretical fit. (f) Simulated SAR distribution (10-g tissue) in a computational model of the human torso at 800 mW continuous power. (g) Temperature change on abdominal skin surface as a function of power after 6 minutes of continuous operation. (h) Temperature change on skin surface as a function of time. Error bars show mean and s.d. of temperature distribution (n = 3 technical trials).

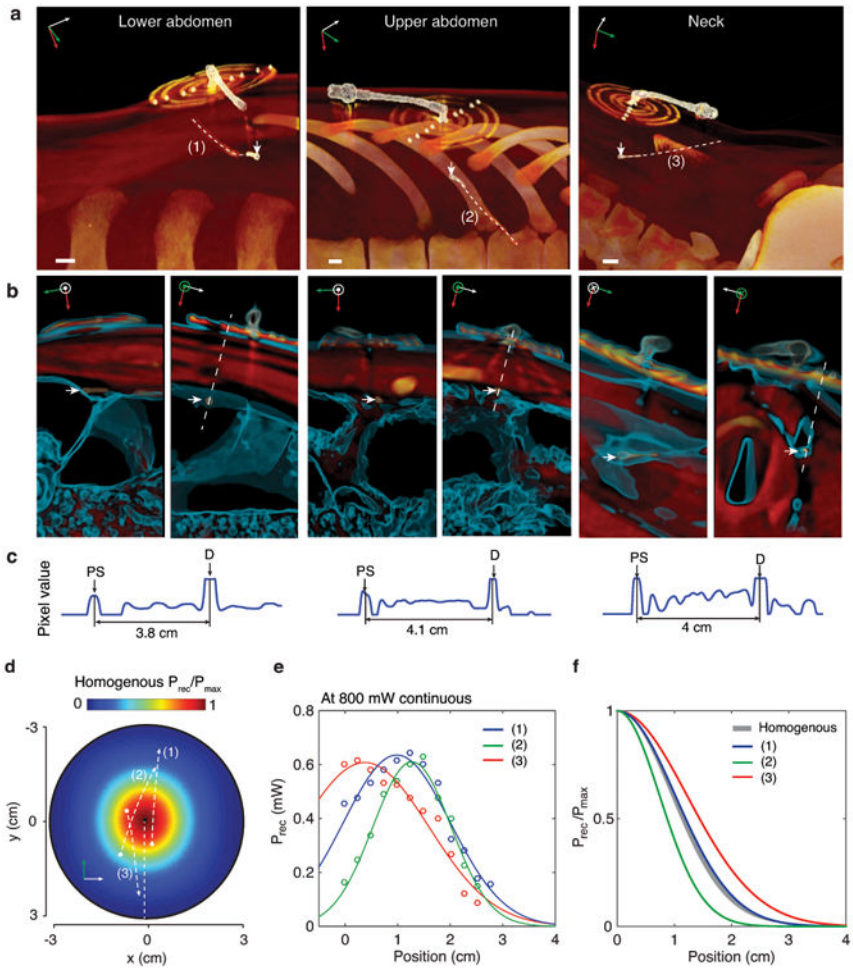

Fig. 4.

Wireless powering of microdevices in pig abdomen and neck. (a) 3D computed tomography (CT) showing the relative position of the phased surface and the microdevice (white arrow) in the peritoneal cavity of the upper and lower abdomen and the carotid sheath in the neck. Local coordinate axis *x* (white), *y* (green), and *z* (red) of the phased surface is shown. The trajectories of the device are labeled (1), (2), and (3) respectively. Scale bar, 1 cm. (b) CT cross-section images with soft tissue contrast. (c) Pixel values along the dotted lines in (b). PS, phased surface; D, device. (d) Trajectory of the microdevice in the transverse (*xy*) plane superimposed on the contour plot of the normalized received power in homogenous tissue 4 cm below the phased surface. (e) Received power as a function of position along the trajectory. Solid lines show Gaussian fit curves. (f) Normalized curves showing widths of the Gaussian fit.

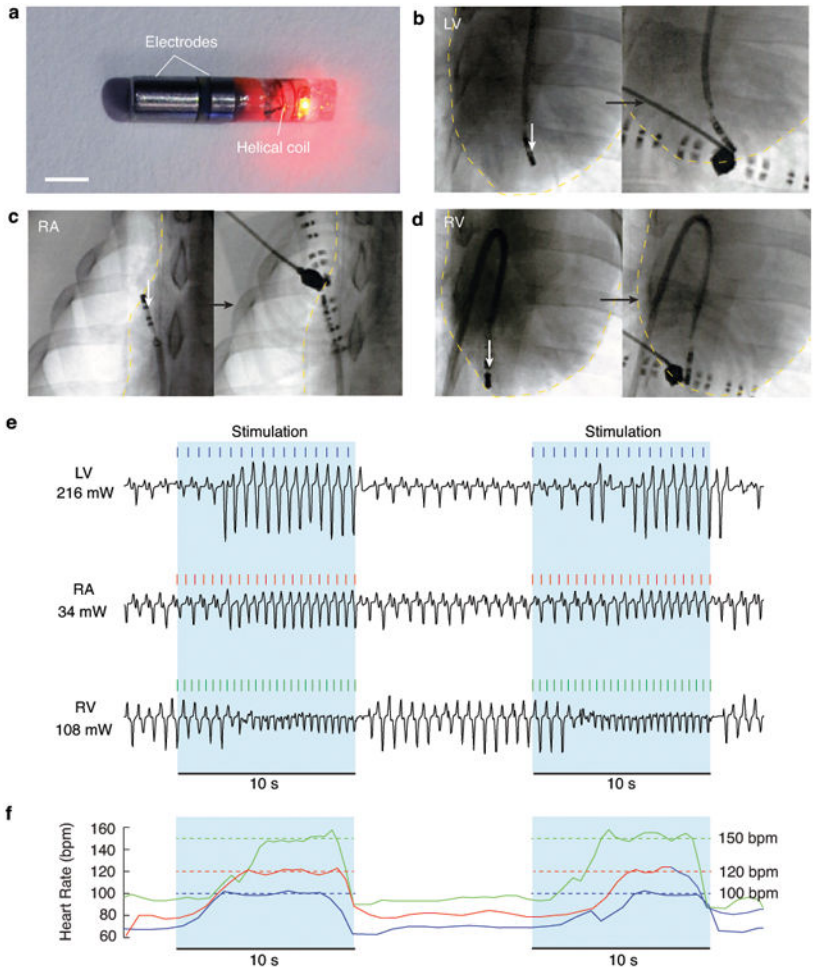

Fig. 5.

In-vivo wireless cardiac pacing in pig. (a) Microdevice configured as a cardiac stimulator. Scale bar, 2 mm. (b, c, d) Projection x-ray image of the stimulator (white arrow) inserted by catheter in the left ventricle (LV), right atrium (RA), and right ventricle (RV) of the heart. For each pair, the image on the right shows the phased surface placed on the chest. (e) Electrocardiogram recording during 10-s stimulation and rest cycles. Stimulation pulse width, 10 ms; period, 600 ms (LV), 500 ms (RA), and 400 ms (RV); average power, 216 mW (LV), 34 mW (RA), and 108 mW (RV). (f) Heart rate during stimulation and rest cycles. Dotted lines show the target heart rate.